

Neural-Network Holographic Model of the QCD Phase Transition under Lattice and HRG Constraints*

De-Xing Zhu,¹ Li-Qiang Zhu,¹ Xun Chen,^{2,3,†} De-Fu Hou,^{1,‡} and Kai Zhou^{4,5,§}

¹*Institute of Particle Physics and Key Laboratory of Quark and Lepton Physics (MOE),
Central China Normal University, Wuhan 430079, China*

²*School of Nuclear Science and Technology, University of South China, Hengyang 421001, China*

³*INFN — Istituto Nazionale di Fisica Nucleare — Sezione di Bari Via Orabona 4, 70125, Bari, Italy*

⁴*School of Science and Engineering, The Chinese University of Hong Kong,
Shenzhen (CUHK-Shenzhen), Guangdong, 518172, China*

⁵*School of Artificial Intelligence, The Chinese University of Hong Kong,
Shenzhen (CUHK-Shenzhen), Guangdong, 518172, China*

Within a neural-network-based holographic framework, we incorporate lattice QCD (LQCD) and Hadron Resonance Gas (HRG) data to train the model and predict the location of the QCD critical endpoint (CEP). The training dataset consists of the entropy density, baryon number susceptibility, and baryon density. The metric warp factor $A(z)$ and the gauge kinetic function $f(z)$ are parameterized by neural networks and determined through the training procedure. The resulting model reproduces the equation of state at vanishing chemical potential in good agreement with both LQCD and HRG data. Extending the analysis to finite chemical potential, we solve the equations of motion and obtain thermodynamic observables consistent with LQCD results at finite density. After incorporating the HRG constraints, the predicted position of the CEP shifts toward larger chemical potentials compared to recent studies. We further employ symbolic regression to derive analytic expressions for $A(z)$ and $f(z)$, providing convenient functional forms for future phenomenological applications. Finally, we perform a data-driven validation using synthetic thermodynamic data generated from an existing analytical holographic model. The neural-network framework reproduces the corresponding CEP location with good accuracy, showing close agreement within numerical uncertainties.

Keywords: Holographic QCD, HRG, Critical endpoint, Neural network

I. INTRODUCTION

Ultra-relativistic heavy-ion collisions performed at the Relativistic Heavy Ion Collider (RHIC) and the Large Hadron Collider (LHC) have provided compelling experimental evidence for the creation of a new state of strongly interacting matter known as the Quark–Gluon Plasma (QGP) [1–15]. Understanding the properties of this strongly interacting QCD matter naturally leads to the investigation of the QCD phase diagram, which remains one of the central frontiers in modern nuclear physics. The transition from hadronic matter to the QGP is governed by non-perturbative dynamics that challenge traditional theoretical methods [16–18]. While perturbative QCD provides accurate predictions at high energy scales, the low-energy regime—characterized by color confinement and chiral symmetry breaking—requires non-perturbative tools. Lattice QCD (LQCD) has successfully

established that the transition at vanishing baryon chemical potential ($\mu_B = 0$) is a smooth crossover [19–21]. However, extending these first-principles calculations to finite baryon density is hindered by the numerical sign problem [22–25], leaving the high-density regime and the potential existence of a Critical Endpoint (CEP) largely unexplored.

AdS/CFT [26–29], offers a powerful complementary approach. Holography maps strongly coupled gauge theories to weakly coupled gravitational theories in a higher-dimensional spacetime. This mapping enables the calculation of quantities – such as thermodynamic observables and transport coefficients – in regimes inaccessible to LQCD [30–32]. Bottom-up holographic models, such as the Einstein-Maxwell-Dilaton (EMD) framework, have been particularly successful in phenomenologically reproducing QCD properties [33–37]. A central challenge in bottom-up holography is the *inverse problem*: determining the precise functional forms of the bulk metric and background fields that correspond to physical QCD data [31, 38]. Traditional approaches rely on parameterized analytical ansätze, such as the Soft-wall model [39].

Recently, machine learning (ML) techniques have been widely applied in high-energy physics [13, 40–45], emerging as powerful tools for tackling complex inverse problems and non-perturbative dynamics. In particular, ML provides a robust data-driven framework for extracting hidden structures from high-dimensional datasets and for constructing effective models beyond traditional analytical approaches. In the context of holographic QCD, several works have attempted to build data-driven holographic models by incorporating LQCD results, experimental measurements, or phe-

* We would like to thank Yan-Qing Zhao and Jia-Hao Wang for helpful discussions. This work is supported in part National Key Research and Development Program of China under Contract No. 2022YFA1604900 and by the National Natural Science Foundation of China (NSFC) Grant No. 12405154, No.92570117, No.12435009 and No. 12275104, Shenzhen Peacock fund under No. 2023TC0179, Ministry of Science and Technology of China under Grant No. 2024YFA1611004, the European Union – Next Generation EU through the research grant number P2022Z4P4B “SOPHYA - Sustainable Optimised PHYSics Algorithms: fundamental physics to build an advanced society” under the program PRIN 2022 PNRR of the Italian Ministero dell’Università e Ricerca (MUR).

† chenxun@usc.edu.cn

‡ houdf@ccnu.edu.cn

§ zhoukai@cuhk.edu.cn

nomenological constraints into neural-network architectures. These studies span a broad range of applications, including meson spectroscopy [46–49], the QCD phase transition and critical phenomena [50–52], shear viscosity in strongly coupled plasma [53], chiral condensate reconstruction [54], and the heavy-quark potential [55, 56]. Additional related developments can be found in [57–62].

In our previous studies, holographic models were constructed through gradient-based parameter optimization constrained by LQCD data [63–65]. Since the Hadron Resonance Gas (HRG) model [66] provides a reliable non-perturbative description of QCD thermodynamics in the confined phase, particularly for $T \lesssim T_c$, it serves as a natural infrared constraint for the equation of state (EoS). Motivated by this complementarity between low- and high-temperature regimes, we develop a data-driven holographic framework that systematically incorporates high-temperature LQCD results together with low-temperature HRG constraints, allowing for a consistent reconstruction of the EoS throughout the (T, μ_B) plane. By employing Physics-Informed Neural Network (PINN) to parameterize the bulk metric and gauge kinetic coupling, we achieve a precise description of the crossover transition without relying on rigid analytical ansätze. Our model predicts the existence of a CEP at $(T_c, \mu_c) = (0.089, 0.922)$ GeV, connecting the smooth crossover at zero density to a first-order phase transition at high density. Additionally, we utilize symbolic regression to derive analytic expressions for the reconstructed background functions, offering a transparent holographic dual for QCD matter. The paper is organized as follows: Section II outlines the EMD formalism and the neural network training methodology. Section III presents the numerical results, including the thermodynamic variables, the phase diagram, and the symbolic regression analysis. Finally, a summary is provided in Section IV.

II. THEORETICAL DESCRIPTIONS

A. Einstein-Maxwell-Dilaton Framework

We employ a bottom-up five-dimensional EMD model to construct the holographic dual of the QCD EoS [50, 63, 67–81]. The action in the Einstein frame is given by:

$$S = \frac{1}{16\pi G_5} \int d^5x \sqrt{-g} \left[R - \frac{f(\phi)}{4} F^2 - \frac{1}{2} \partial_\mu \phi \partial^\mu \phi - V(\phi) \right], \quad (1)$$

where G_5 is the five-dimensional Newton constant. ϕ is the dilaton field, which is used to break the conformal symmetry. $V(\phi)$ is the potential, and $f(\phi)$ is the gauge kinetic function coupling the Maxwell field A_μ to the background geometry. We treat the gauge coupling $f(\phi)$ as a dynamical function of the holographic coordinate, to be determined via data-driven reconstruction.

The metric ansatz is chosen as:

$$ds^2 = \frac{L^2 e^{2A(z)}}{z^2} \left[-g(z) dt^2 + \frac{dz^2}{g(z)} + d\vec{x}^2 \right], \quad (2)$$

where z is the holographic coordinate ($z = 0$ is the boundary), and $L = 1$ is the AdS radius. The function $A(z)$ is the warp factor. The blackening function $g(z)$ determines the horizon location z_h via $g(z_h) = 0$.

B. Neural Network Reconstruction

To faithfully reproduce the LQCD EoS without relying on ad-hoc analytical ansätze, we employ the PINN approach. We utilize two independent neural networks to reconstruct the background geometry and the gauge sector:

1. Metric Network: The warp factor $A(z)$ is parameterized as:

$$A(z) = z^2 \cdot \mathcal{N}_A(z; \theta_A), \quad (3)$$

where \mathcal{N}_A is a neural network and the factor z^2 ensures the UV boundary condition $A(0) = 0$ is strictly satisfied.

2. Gauge Network: The gauge kinetic function $f(z)$ which governs the coupling between the background geometry and the baryon density, is parameterized by a second independent neural network:

$$f(z) = \mathcal{N}_f(z; \theta_f). \quad (4)$$

This allows the model to learn the non-trivial density dependence implicitly contained in the lattice baryon susceptibility χ_2^B , without restricting the solution space to a specific analytical class. Once $A(z)$ and $f(z)$ are fixed by the networks, the remaining background functions $g(z)$ and $A_t(z)$ are derived by solving the Einstein-Maxwell equations.

$$\begin{aligned} \phi'(z) &= \sqrt{6(A'^2 - A'' - 2A'/z)}, \\ g(z) &= 1 + \frac{1}{\int_0^{z_h} y^3 e^{-3A} dy} \left[-\int_0^z y^3 e^{-3A} dy + \left(\frac{\mu}{\int_0^{z_h} \frac{y}{e^A f} dy} \right)^2 \hat{G} \right], \\ A_t(z) &= \mu \frac{\int_{z_h}^z \frac{y}{e^A f} dy}{\int_{z_h}^0 \frac{y}{e^A f} dy}, \\ V(z) &= -3z^2 g e^{-2A} \left[A'' + A' \left(3A' - \frac{6}{z} + \frac{3g'}{2g} \right) - \frac{1}{z} \left(-\frac{4}{z} + \frac{3g'}{2g} \right) + \frac{g''}{6g} \right], \end{aligned} \quad (5)$$

where μ is the chemical potential. The expression of \hat{G} is

$$\hat{G} = \left| \begin{array}{cc} \int_0^{z_h} y^3 e^{-3A} dy & \int_0^{z_h} y^3 e^{-3A} dy \int_0^y \frac{x}{e^A f} dx \\ \int_{z_h}^z y^3 e^{-3A} dy & \int_{z_h}^z y^3 e^{-3A} dy \int_0^y \frac{x}{e^A f} dx \end{array} \right|. \quad (6)$$

C. Thermodynamics and Conserved Quantities

The thermodynamic observables of the boundary system are established through the holographic dictionary. Consequently, the temperature T , entropy density s , and baryon number density ρ evaluate to:

$$T = \frac{1}{4\pi} \frac{z_h^3 e^{-3A(z_h)}}{\int_0^{z_h} y^3 e^{-3A(z)} dy} \left[1 - \left(\frac{\mu}{\int_0^{z_h} \frac{y}{e^A f} dy} \right)^2 \right. \\ \left. \left(\int_0^{z_h} y^3 e^{-3A} dy \cdot \int_0^{z_h} \frac{x}{e^A f} dx \right. \right. \\ \left. \left. - \int_0^{z_h} y^3 e^{-3A} dy \int_0^y \frac{x}{e^A f} dx \right) \right], \quad (7)$$

$$s = \frac{e^{3A(z_h)}}{4G_5 z_h^3},$$

$$\rho = \frac{1}{16\pi G_5} \frac{\mu}{\int_0^{z_h} \frac{y}{e^A f} dy}.$$

Given the entropy and density ρ , the free energy and pressure follow from integration of the appropriate thermodynamic identity [64, 82].

$$dF = -dp = -s dT - \rho d\mu. \quad (8)$$

The free energy is normalized to zero at $(T, \mu) = (0, 0)$. With this convention, the energy density can be expressed as

$$\epsilon = -p + sT + \mu\rho. \quad (9)$$

We also consider the trace anomaly

$$I = \epsilon - 3p. \quad (10)$$

The specific heat at constant volume is computed from the entropy [35],

$$C_V = T \left(\frac{\partial s}{\partial T} \right)_\mu. \quad (11)$$

The squared speed of sound for systems with non-zero chemical potential is obtained via [83–85]

$$C_s^2 = \frac{s}{T \left(\frac{\partial s}{\partial T} \right)_\mu + \mu \left(\frac{\partial \rho}{\partial T} \right)_\mu}. \quad (12)$$

The second-order baryon number susceptibility is defined as

$$\chi_2^B = \frac{1}{T^2} \frac{\partial \rho}{\partial \mu}. \quad (13)$$

The thermodynamic consistency of our Neural-Network Holographic Model (NNHM) is rigorously examined through the behavior of these derived quantities.

D. Training Strategy

The NNHM are optimized by minimizing a total loss function \mathcal{L} that quantifies the deviation from LQCD data. The training process integrates data from both zero and finite chemical potentials:

1. Metric Training ($\mu = 0$): \mathcal{N}_A is trained using entropy density $s(T)$ at vanishing chemical potential.
2. Gauge Training ($\mu \neq 0$): \mathcal{N}_f is trained using baryon number susceptibility $\chi_2^B(T)$ at $\mu = 0$ and baryon density $\rho(T, \mu)$ at $\mu_B/T = 1$.

To address the scarcity of lattice data in the low-temperature regime, we augment the training dataset with HRG model predictions for $T < 0.13$ GeV. This hybrid dataset ensures that the neural network learns the correct hadronic degrees of freedom, thereby determining more precise thermodynamic properties.

III. RESULTS AND DISCUSSION

A fundamental challenge in bottom-up holographic QCD is the construction of a bulk geometry that simultaneously captures the physics of the deconfined QGP and the confined hadronic phase within a unified framework. Traditional models often rely on hand-crafted analytical ansätze for the warp factor $A(z)$ or dilaton potential $V(\phi)$, which inherently introduces human-imposed bias and often fails to reproduce the hadronic limit at low temperatures ($T \leq 0.13$ GeV).

In this work, we implement a data-to-holography pipeline that solves the inverse problem by treating $A(z)$ and the gauge-dilaton coupling $f(z)$ as deep-learning-optimized functional profiles. To anchor the model across the entire phase space, we adopt a hybrid training strategy: (2+1)-flavor LQCD data [18, 86] is used for the high-temperature regime. For the low-temperature region, where lattice calculations encounter computational bottlenecks, the model is constrained by predictions from the HRG model, these predictions are generated using the Thermal-FIST package [87], a C++-based software tool specifically designed for studying heavy-ion collisions and hadronic equations of state.

A. Thermodynamic Validation at $\mu_B = 0$

At vanishing chemical potential, our machine-learning augmented EMD model demonstrates quantitative agreement with first-principles thermodynamics. As shown in Fig. 1, where we present the temperature dependence of the thermodynamic EoS at vanishing baryon chemical potential, the normalized pressure p , energy density ϵ , and entropy density s align closely with lattice benchmarks across the range $0.13 \text{ GeV} \leq T \leq 0.60 \text{ GeV}$.

Crucially, the model captures the non-conformal behavior of the crossover transition. The speed of sound squared C_s^2 exhibits a characteristic dip near $T \approx 0.15$ GeV, representing

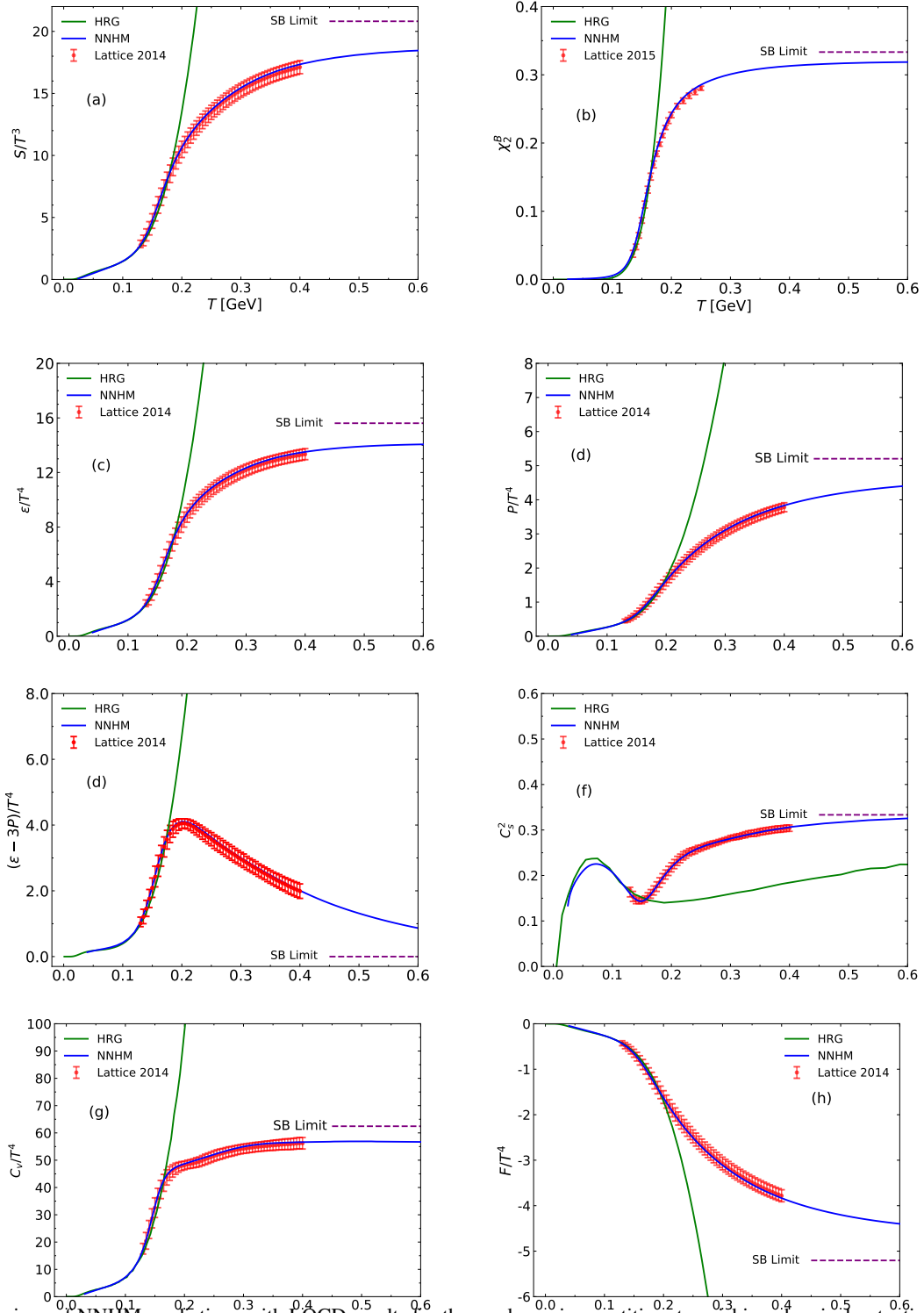


Fig. 1. Comparison of NNHM predictions with LQCD results for thermodynamic quantities at vanishing chemical potential. The blue solid lines represent the NNHM results, while the red points with error bars denote the (2+1)-flavor LQCD data from Ref. [18, 86]. For reference, the green solid lines show the HRG model calculations, and the purple dashed lines indicate the SB limits. The plotted quantities are: entropy density s , energy density ϵ , pressure P , trace anomaly $\epsilon - 3P$, second-order baryon susceptibility χ_2^B , squared speed of sound C_s^2 , specific heat C_V , and free energy F , all appropriately scaled by powers of temperature T .

the “softest point” of the EoS. While pure HRG models diverge significantly beyond this region as they fail to account for deconfined degrees of freedom, our model correctly below the Stefan–Boltzmann (SB) limit at high temperatures. As shown in Fig. 1, the NNHM prediction serves as a robust bridge between the low-temperature hadronic phase and the high-temperature QGP. The smooth interpolation from the hadronic dip to the conformal limit ($C_s^2 \rightarrow 1/3$) confirms that the neural network parameterization of $f(z)$ does not introduce spurious oscillations. Furthermore, the second-order baryon susceptibility χ_2^B is well-reproduced, validating that the learned coupling $f(z)$ accurately reflects the system’s sensitivity to density fluctuations.

B. Finite Density Extrapolation and Susceptibility Response

By extending the neural-network-determined $A(z)$ and $f(z)$ to finite chemical potential, we investigate the system’s response to increasing baryon density for chemical potential-to-temperature ratios up to $\mu_B/T = 2.5$. We observe a monotonic enhancement in all extensive thermodynamic observables, consistent with the physical expectation of increased quark populations at higher chemical potentials.

The robustness of this extrapolation is cross-verified against lattice Taylor expansion and Padé approximant results at small μ_B . For ratios $\mu_B/T = 1.0$ and 1.5 , the holographic predictions for the scaled baryon density ρ/T^3 and susceptibility χ_2^B exhibit broad consistency with lattice estimates. While minor deviations are observed in the magnitude of the baryon susceptibility and energy density at intermediate temperatures (as seen in Fig. 2 (b) and (d)), the model successfully captures the critical qualitative trends: the rapid rise of thermal quantities near T_c and the correct asymptotic behavior.

C. Localization of the CEP and Phase Structure

The central objective of this work is the precise mapping of the QCD phase structure across the (T, μ_B) plane. To delineate the phase boundaries, we track two distinct thermodynamic indicators: the local minimum of the squared speed of sound (C_s^2), which signifies the softening of the EoS, and the inflection point of the scaled entropy density (s/T^3), which traces the rapid liberation of degrees of freedom.

In the regime of low baryon chemical potential, these two pseudo-critical lines remain distinct, bounding a crossover region of finite width. As the baryon chemical potential increases, the separation between the pseudo-critical lines decreases. They approach each other and become indistinguishable near a singular point, signaling the termination of the crossover region and the emergence of a first-order phase transition line. Based on our optimized holographic reconstruction (as shown by the red dots in Fig. 3), we localize the CEP at:

$$T_c = 0.089 \text{ GeV}, \quad \mu_c = 0.922 \text{ GeV}. \quad (14)$$

For baryon chemical potentials beyond the CEP ($\mu_B > \mu_c$), the system undergoes a first-order phase transition characterized by discontinuous jumps in entropy density and baryon density. The corresponding coexistence line extends toward the zero-temperature axis, terminating at a critical chemical potential of approximately $\mu_B \approx 1.6 \text{ GeV}$ at $T = 0$.

This topological structure is qualitatively consistent with predictions from functional approaches, including the Functional Renormalization Group (FRG) [91–96] and Dyson–Schwinger Equations (DSE) [97–100]. Compared with previous holographic studies, the CEP obtained in our model appears at a larger chemical potential due to the inclusion of HRG constraints. To illustrate this effect, several representative results are shown in Fig. 3. The brown hexagon denotes a potential-reconstruction EMD model, which lies close to the $V(\phi)$ EMD model represented by the orange triangle [90]. The purple square corresponds to the merged EoS model incorporating both LQCD and HRG data [90]. These comparisons demonstrate that the inclusion of HRG data significantly shifts the CEP location toward larger baryon chemical potential within the holographic framework.

D. Analytic Reconstruction via Symbolic Regression

To interpret the numerical solutions generated by the neural networks, we employ symbolic regression (via PySR) to extract precise analytic forms for the warp factor $A(z)$ and gauge kinetic function $f(z)$. This process transforms the “black-box” output into transparent algebraic expressions.

The symbolic regression was implemented using genetic programming algorithms to search the functional space for expressions that minimize the mean squared error while maximizing simplicity. To strictly enforce holographic boundary conditions, we applied domain-specific pre-processing: for the warp factor, the regression target was transformed to $A(z)/z$ to guarantee the linear asymptotic behavior $A(z) \sim z$ near the AdS boundary ($z \rightarrow 0$). For the gauge kinetic term, we fitted the logarithm $\log(f(z)/f_0)$ to ensure the function remains positive definite. Furthermore, we imposed a custom weighting scheme, $w(z)$, which heavily penalizes errors in the UV region ($z < 0.2$) to preserve the accuracy of the perturbative slope. The search space was restricted to fundamental arithmetic operators $\{+, -, \times, \div, \text{square}\}$ and excluded general power laws, thereby forcing the algorithm to find analytic rational or exponential structures rather than unphysical fractional approximations.

The resulting analytic expressions achieve remarkable consistency with the numerical data ($R^2 > 0.999$). Crucially, these forms explicitly reveal the pole structures in the bulk geometry that drive the confinement-deconfinement transition. The reconstructed functions are:

$$A(z) = z \left[\left(a + \frac{b}{c - (z + \frac{d}{z})} \right) (z + e) \right] \quad (15)$$

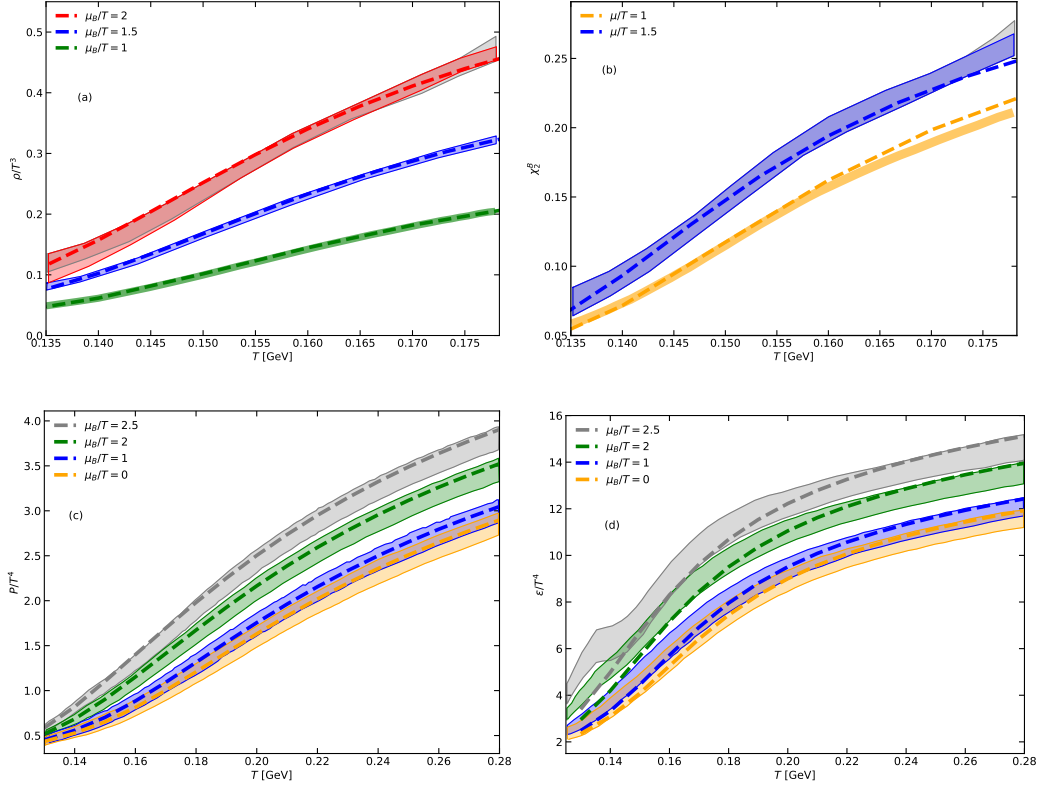


Fig. 2. Comparison of NNHM predictions with (2+1)-flavor LQCD results for the thermodynamic EoS at finite chemical potential, the shadow region represents the LQCD results, while the dashed line shows the calculations from NNHM. The panels display the temperature dependence of: (a) scaled baryon number density ρ/T^3 , (b) second-order baryon susceptibility χ_2^B , (c) scaled pressure P/T^4 , and (d) scaled energy density ϵ/T^4 . The LQCD data are taken from Ref. [88] (for ρ and χ_2^B) and Ref. [89] (for ϵ and P).

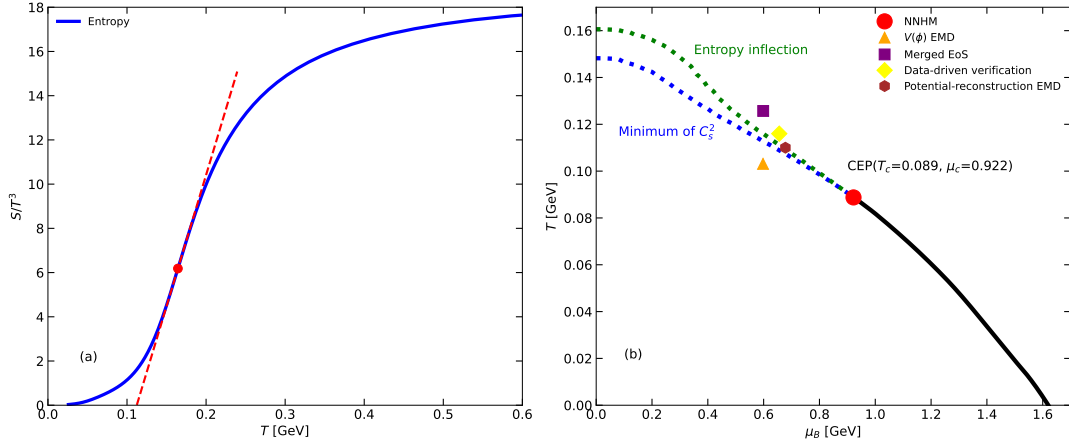


Fig. 3. QCD phase structure obtained within the data-driven NNHM. (a) Determination of the pseudo-critical temperature from the entropy density, where the inflection point of s/T^3 is identified through the tangent construction. (b) The QCD phase diagram in the T - μ_B plane. The crossover region is bounded by two pseudo-critical indicators: the minimum of the squared speed of sound (C_s^2 , blue dotted line) and the entropy inflection line (green dotted line). These lines become indistinguishable at the CEP, located at $(T, \mu_B) = (0.089, 0.922)$ GeV (red circle), beyond which a first-order phase transition line (solid black curve) emerges. For comparison, CEP estimates from the $V(\phi)$ EMD model (orange triangle) [90], the merged equation-of-state model including LQCD and HRG constraints (purple square) [90], and a potential-reconstruction EMD model (brown hexagon) are shown [65]. The yellow diamond represents a synthetic-data benchmark, in which thermodynamic data generated from a known analytical EMD model are used to train the NNHM, demonstrating that the neural network can reproduce the corresponding CEP location within numerical uncertainties and confirming the data-driven nature of the reconstruction.

1

$$f(z) = f_0 \exp \left[f + \frac{g}{h \left(i + \frac{1}{j-z^2} \right)^2 + k} \right] \quad (16)$$

The corresponding parameters are listed in Table 1, and the comparison with the numerical results is shown in Fig. 4.

TABLE 1. Analytical parameters for the warp factor $A(z)$ and the gauge kinetic function $f(z)$ reconstructed via symbolic regression. The functional forms are constrained to rational and exponential structures to satisfy holographic boundary conditions. Parameters a – e define the rational structure of $A(z)$, while f_0 and f – k characterize the normalization and near-horizon behavior of $f(z)$.

Parameter	Value	Parameter	Value
a	4.83×10^{-4}	f	0.0403
b	6.16×10^{-2}	g	7.40
c	3.30	h	−134
d	11.7	i	0.00743
e	2.74	j	0.885
f_0	0.33448	k	−1.55

E. Three-Dimensional Structure of the QCD Equation of State

Based on the analytically reconstructed warp factor $A(z)$ and gauge kinetic function $f(z)$, we evaluate the thermodynamic observables over the full (T, μ_B) plane. The corresponding three-dimensional profiles are displayed in Fig. 5, including the entropy density, baryon number susceptibility, energy density, pressure, trace anomaly, squared speed of sound, specific heat, and baryon density. These surfaces provide a global view of the EoS at finite temperature and finite baryon chemical potential.

As shown in Fig. 5, the extensive thermodynamic quantities, including s/T^3 , ϵ/T^4 , p/T^4 , C_V/T^3 , and ρ/T^3 , generally increase with increasing chemical potential, especially in the low-temperature region. This behavior reflects the enhanced population of baryonic degrees of freedom at finite density.

The trace anomaly $(\epsilon - 3p)/T^4$ develops a pronounced structure in the low- T , high- μ_B region, indicating stronger non-conformal dynamics there. In contrast, the squared speed of sound C_s^2 exhibits a nontrivial suppression around the crossover region and becomes softer as the system approaches the phase boundary, which is consistent with the expected softening of the EoS near criticality.

The baryon number susceptibility χ_2^B and the baryon density ρ/T^3 show particularly strong responses to finite chemical potential, demonstrating that the reconstructed gauge sector captures the density dependence of the system in a thermodynamically consistent manner. Overall, the smooth but nontrivial structures of these surfaces support the reliability of the neural-network holographic reconstruction in describing QCD thermodynamics across a broad region of the phase diagram.

F. Data-driven verification

To explicitly demonstrate that the neural network does not introduce spurious bias, we perform a benchmark reconstruction using synthetic data. A natural concern in machine-learning-assisted holography is whether the predicted CEP location (or even its existence) could be an artifact of the chosen neural architecture rather than being dictated by the input thermodynamics. To address this, we feed the same NNHM training pipeline with synthetic thermodynamic data—specifically the entropy density s , the second-order baryon susceptibility χ_2^B , and the baryon density ρ generated from the analytical EMD model used in our previous work [65]. As indicated by the yellow diamond in Fig. 3, the neural network accurately reproduces the CEP of that reference model. This consistency check confirms that the NNHM acts as an unbiased functional mapper: the trajectories of the pseudo-critical lines and their convergence at the CEP are dictated by the physics encoded in the input data rather than by restrictive parametric assumptions.

Quantitatively, the CEP (yellow diamond) extracted from data generated by the potential-reconstruction EMD model is located at $(T_c, \mu_c) = (0.116, 0.656)$ GeV, which is close to the value obtained in the original model, $(T_c, \mu_c) = (0.110, 0.678)$ GeV, reported in Ref. [65], within the expected numerical uncertainties. This agreement supports the reliability of our reconstruction pipeline and indicates that the CEP prediction of the NNHM is genuinely data-driven.⁵

IV. SUMMARY

In this work, we developed a neural-network-based holographic reconstruction of the QCD EoS across the (T, μ_B) plane by combining high-temperature LQCD inputs with low-temperature constraints from the Hadron Resonance Gas (HRG) model. Within a bottom-up Einstein–Maxwell–Dilaton (EMD) framework, the metric warp factor $A(z)$ and the gauge kinetic function $f(z)$ were parameterized by neural networks and optimized using thermodynamic observables, providing a flexible and data-driven solution to the holographic inverse problem without relying on restrictive analytic ansätze.

At vanishing baryon chemical potential, the reconstructed model reproduces the lattice EoS and captures the non-conformal features of the QCD crossover, while remaining consistent with HRG thermodynamics in the confined phase. Extending the analysis to finite baryon chemical potential, we obtained a self-consistent set of thermodynamic observables and mapped the QCD phase structure using the minima of the squared speed of sound C_s^2 and the inflection points of the scaled entropy density s/T^3 as pseudo-critical indicators. The resulting phase diagram exhibits a finite-width crossover region at small μ_B , which terminates at a critical endpoint

⁵ The code can be found at: <https://github.com/De-Xing-Zhu/>

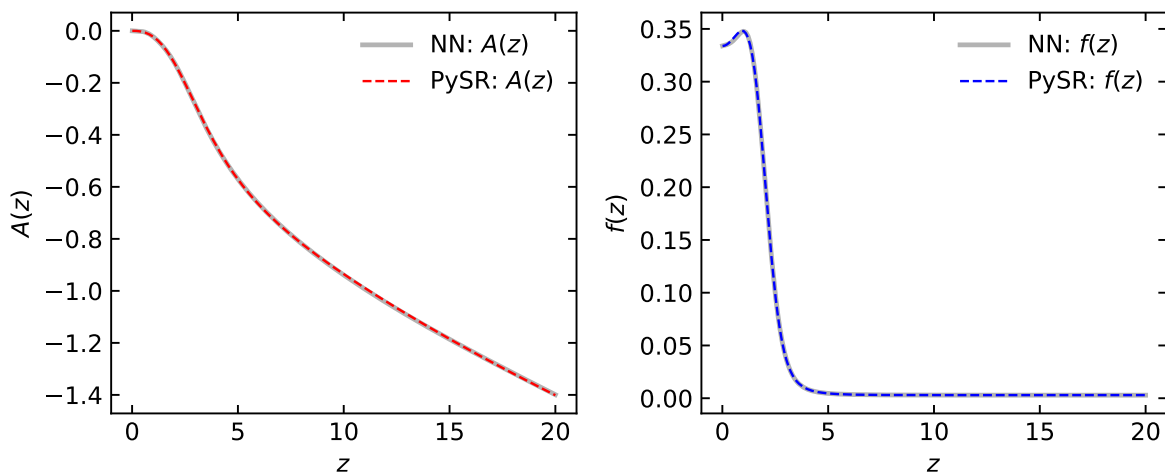


Fig. 4. Comparison of the neural-network numerical solutions (gray solid lines) with the analytical expressions obtained from symbolic regression (colored dashed lines). The left panel displays the warp factor $A(z)$, while the right panel shows the gauge kinetic function $f(z)$. The nearly perfect overlap ($R^2 > 0.999$) demonstrates that the derived analytical formulas capture the essential nonlinear dynamics and pole structures of the holographic model.

located at $(T_c, \mu_c) = (0.089, 0.922)$ GeV, beyond which a first-order transition line emerges.

To visualize the global thermodynamic structure of the reconstructed model, we further constructed three-dimensional surfaces of the EoS across the (T, μ_B) plane, including the entropy density, baryon density, pressure, energy density, trace anomaly, speed of sound, and specific heat. These surfaces provide a comprehensive view of the density dependence of QCD thermodynamics and illustrate the softening behavior of the EoS in the vicinity of the phase-transition region.

To improve the interpretability of the neural-network reconstruction, we applied symbolic regression to extract compact analytic expressions for the background functions $A(z)$ and $f(z)$, achieving excellent agreement with the numerical solutions. Finally, a synthetic-data benchmark based on an analytical EMD model demonstrates that the reconstruction pipeline can faithfully recover the corresponding critical endpoint, confirming that the predicted phase structure is primarily determined by the input thermodynamic data rather than by model assumptions.

However, several limitations must be acknowledged. First, the reconstruction's fidelity is inherently tied to the quality and scope of the input data. While we used state-of-the-art lattice results at $\mu_B = 0$, the constraints at finite μ_B are indirect, derived from the neural network's interpolation/extrapolation based on the zero-density training and the HRG boundary condition. The absence of direct, precise lattice data at finite μ_B remains a fundamental challenge. Second, the EMD framework, while versatile, incorporates a spe-

cific set of fields (gravity, a $U(1)$ gauge field for baryon number, and a dilaton for running coupling). It does not explicitly include chiral symmetry breaking, which is a key aspect of the QCD transition. The phase structure we identify is therefore primarily associated with deconfinement and thermodynamic crossover/transition, as probed by bulk observables like the speed of sound. Third, the symbolic regression, while successful in providing interpretable analytic forms for $A(z)$ and $f(z)$, yields approximations. The excellent agreement with numerical results is encouraging, but the expressions may not capture all nuances in regions with sparse data constraints.

In conclusion, we have established a powerful, flexible, and data-driven pipeline for holographic QCD thermodynamics. By leveraging neural networks to solve the inverse problem, we obtained a comprehensive model that reproduces known lattice results, predicts a phase structure featuring a critical endpoint, and provides global thermodynamic surfaces. The synergy between holography and machine learning demonstrated here offers a compelling paradigm for extracting the gravitational dual of complex quantum field theories from empirical and ab initio data, paving the way for a more rigorous and data-informed application of gauge/gravity duality to strong interaction physics.

Overall, this work highlights the potential of machine-learning-assisted holographic approaches as a data-driven framework for exploring the QCD phase diagram. Future developments may incorporate more precise lattice data and additional QCD observables, which could further constrain the holographic background and lead to a more reliable determination of the thermodynamic properties of strongly interacting matter.

[1] K. Adcox et al. Formation of dense partonic matter in relativistic nucleus-nucleus collisions at RHIC: Experimental

evaluation by the PHENIX collaboration. *Nucl. Phys. A*,

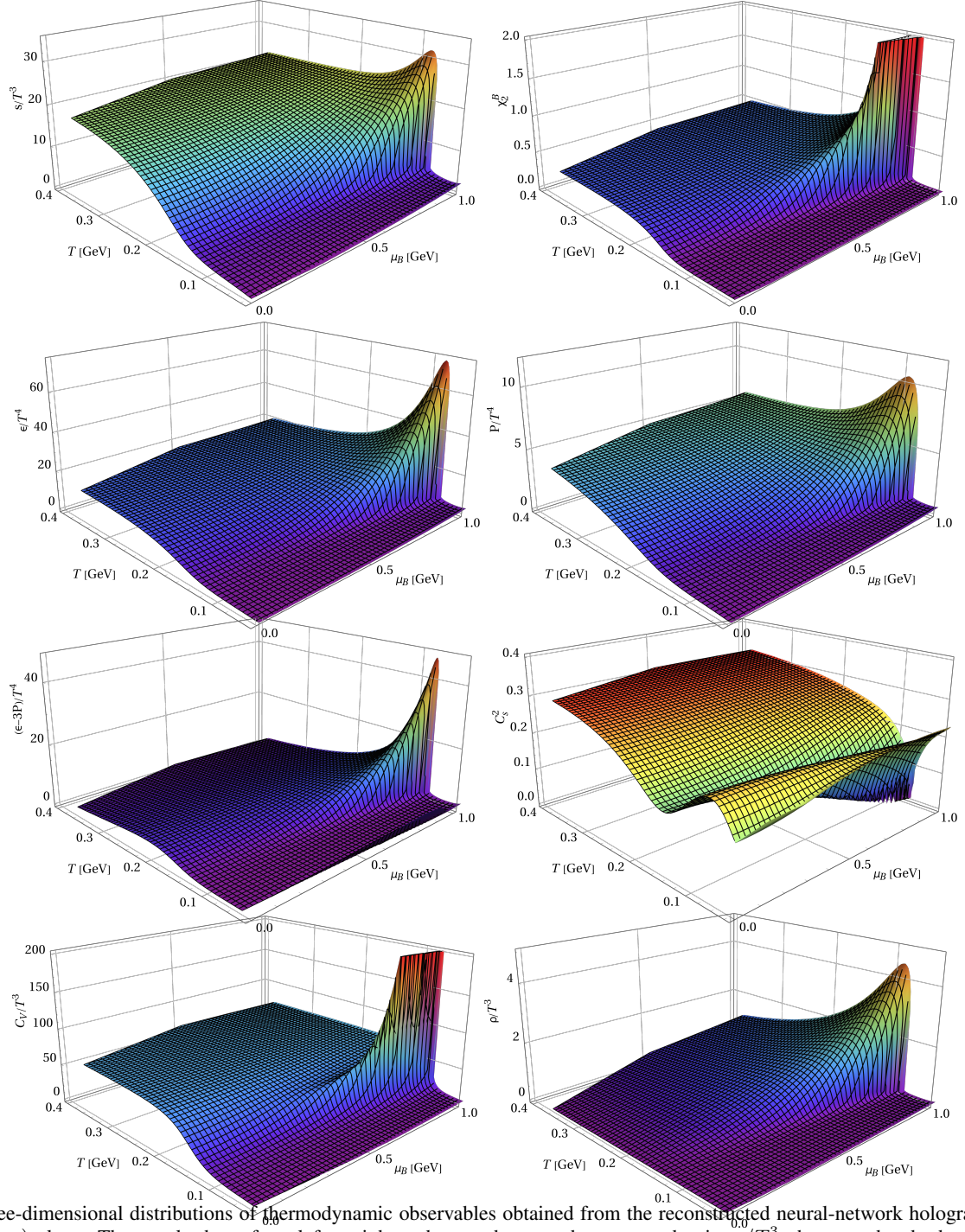


Fig. 5. Three-dimensional distributions of thermodynamic observables obtained from the reconstructed neural-network holographic model on the (T, μ_B) plane. The panels show, from left to right and top to bottom, the entropy density s/T^3 , the second-order baryon number susceptibility χ_2^B , the energy density ϵ/T^4 , the pressure p/T^4 , the trace anomaly $(\epsilon - 3p)/T^4$, the squared speed of sound C_s^2 , the specific heat C_V/T^3 , and the baryon number density ρ/T^3 . These surface plots illustrate the global thermodynamic structure of the model at finite temperature and baryon chemical potential, and provide a direct visualization of the nontrivial density dependence.

757:184–283, 2005.

- [2] M. M. Aggarwal et al. An Experimental Exploration of the QCD Phase Diagram: The Search for the Critical Point and the Onset of De-confinement. 7 2010.
- [3] Jinhui Chen et al. Properties of the QCD matter: review of selected results from the relativistic heavy ion collider beam energy scan (RHIC BES) program. *Nucl. Sci. Tech.*, 35(12):214,

2024.

- [4] Hai Wang and Jin-Hui Chen. Anisotropy flows in Pb–Pb collisions at LHC energies from parton scatterings with heavy quark trigger. *Nucl. Sci. Tech.*, 33(2):15, 2022.
- [5] Hai Wang and Jin-Hui Chen. Study on open charm hadron production and angular correlation in high-energy nuclear collisions. *Nucl. Sci. Tech.*, 32(1):2, 2021.

- [6] Hai Wang, Jin-Hui Chen, Yu-Gang Ma, and Song Zhang. Charm hadron azimuthal angular correlations in Au + Au collisions at $\sqrt{s_{NN}} = 200$ GeV from parton scatterings. *Nucl. Sci. Tech.*, 30(12):185, 2019.
- [7] Zhi-Wan Xu, Song Zhang, Yu-Gang Ma, Jin-Hui Chen, and Chen Zhong. Influence of α -clustering nuclear structure on the rotating collision system. *Nucl. Sci. Tech.*, 29(12):186, 2018.
- [8] Xiao-Hai Jin, Jin-Hui Chen, Yu-Gang Ma, Song Zhang, Chun-Jian Zhang, and Chen Zhong. Ω and ϕ production in Au + Au collisions at $\sqrt{s_{NN}} = 11.5$ and... *Nucl. Sci. Tech.*, 29(4):54, 2018.
- [9] Peng Liu, Jin-Hui Chen, Yu-Gang Ma, and Song Zhang. Production of light nuclei and hypernuclei at High Intensity Accelerator Facility energy region. *Nucl. Sci. Tech.*, 28(4):55, 2017. [Erratum: *Nucl. Sci. Tech.* 28, 89 (2017)].
- [10] Liqiang Zhu, Zhan Gao, Weiyao Ke, and Hanzhong Zhang. Bayesian inference of the magnetic field and chemical potential on holographic jet quenching in heavy-ion collisions. 5 2025.
- [11] Yao Li, Shuwan Shen, Sa Wang, and Ben-Wei Zhang. Transverse momentum balance of dijets in Xe+Xe collisions at the LHC. *Nucl. Sci. Tech.*, 35(7):113, 2024.
- [12] Man Xie, Qing-Fei Han, En-Ke Wang, Ben-Wei Zhang, and Han-Zhong Zhang. The medium-temperature dependence of jet transport coefficient in high-energy nucleus–nucleus collisions. *Nucl. Sci. Tech.*, 35(7):125, 2024.
- [13] Wan-Bing He, Yu-Gang Ma, Long-Gang Pang, Hui-Chao Song, and Kai Zhou. High-energy nuclear physics meets machine learning. *Nucl. Sci. Tech.*, 34(6):88, 2023.
- [14] Jin-Hui Chen, Jinhui Chen, Feng-Kun Guo, Yu-Gang Ma, Cheng-Ping Shen, Qi-Ye Shou, Qiye Shou, Qian Wang, Jia-Jun Wu, and Bing-Song Zou. Production of exotic hadrons in pp and nuclear collisions. *Nucl. Sci. Tech.*, 36(4):55, 2025.
- [15] Yi-Fei Xu, Yong-Jin Ye, Jin-Hui Chen, Yu-Gang Ma, Song Zhang, and Chen Zhong. Low-mass vector meson production at forward rapidity in p+p and d+Au collisions at $\sqrt{s_{NN}} = 200$ GeV from a multiphase transport model. *Nucl. Sci. Tech.*, 27(4):87, 2016.
- [16] Jana N. Guenther. Overview of the QCD phase diagram: Recent progress from the lattice. *Eur. Phys. J. A*, 57(4):136, 2021.
- [17] Gert Aarts et al. Phase Transitions in Particle Physics: Results and Perspectives from Lattice Quantum Chromo-Dynamics. *Prog. Part. Nucl. Phys.*, 133:104070, 2023.
- [18] A. Bazavov et al. Equation of state in (2+1)-flavor QCD. *Phys. Rev. D*, 90:094503, 2014.
- [19] Y. Aoki, G. Endrodi, Z. Fodor, S. D. Katz, and K. K. Szabo. The Order of the quantum chromodynamics transition predicted by the standard model of particle physics. *Nature*, 443:675–678, 2006.
- [20] S. Borsanyi, Z. Fodor, S. D. Katz, S. Krieg, C. Ratti, and K. K. Szabo. Freeze-out parameters: lattice meets experiment. *Phys. Rev. Lett.*, 111:062005, 2013.
- [21] Alexander Adam, Szabolcs Borsanyi, Zoltan Fodor, Jana N. Guenther, Piyush Kumar, Paolo Parotto, Attila Pásztor, and Chik Him Wong. High-precision baryon number cumulants from lattice QCD in a finite box: cumulant ratios, Lee-Yang zeros and critical endpoint predictions. 7 2025.
- [22] Owe Philipsen. The QCD equation of state from the lattice. *Prog. Part. Nucl. Phys.*, 70:55–107, 2013.
- [23] Gert Aarts. Introductory lectures on lattice QCD at nonzero baryon number. *J. Phys. Conf. Ser.*, 706(2):022004, 2016.
- [24] Keitaro Nagata. Finite-density lattice QCD and sign problem: Current status and open problems. *Prog. Part. Nucl. Phys.*, 127:103991, 2022.
- [25] Philippe de Forcrand. Simulating QCD at finite density. *PoS, LAT2009:010*, 2009.
- [26] Juan Martin Maldacena. The Large N limit of superconformal field theories and supergravity. *Adv. Theor. Math. Phys.*, 2:231–252, 1998.
- [27] Edward Witten. Anti de Sitter space and holography. *Adv. Theor. Math. Phys.*, 2:253–291, 1998.
- [28] S. S. Gubser, Igor R. Klebanov, and Alexander M. Polyakov. Gauge theory correlators from noncritical string theory. *Phys. Lett. B*, 428:105–114, 1998.
- [29] Ofer Aharony, Steven S. Gubser, Juan Martin Maldacena, Hiroshi Ooguri, and Yaron Oz. Large N field theories, string theory and gravity. *Phys. Rept.*, 323:183–386, 2000.
- [30] Romulo Rougemont, Joaquin Grefa, Mauricio Hippert, Jorge Noronha, Jacquelyn Noronha-Hostler, Israel Portillo, and Claudia Ratti. Hot QCD phase diagram from holographic Einstein–Maxwell–Dilaton models. *Prog. Part. Nucl. Phys.*, 135:104093, 2024.
- [31] Joaquin Grefa, Jorge Noronha, Jacquelyn Noronha-Hostler, Israel Portillo, Claudia Ratti, and Romulo Rougemont. Hot and dense quark-gluon plasma thermodynamics from holographic black holes. *Phys. Rev. D*, 104(3):034002, 2021.
- [32] Romulo Rougemont, Andrej Ficnar, Stefano Finazzo, and Jorge Noronha. Energy loss, equilibration, and thermodynamics of a baryon rich strongly coupled quark-gluon plasma. *JHEP*, 04:102, 2016.
- [33] U. Gursoy, E. Kiritsis, and F. Nitti. Exploring improved holographic theories for QCD: Part II. *JHEP*, 02:019, 2008.
- [34] Umut Gursoy, Elias Kiritsis, Liuba Mazzanti, and Francesco Nitti. Deconfinement and Gluon Plasma Dynamics in Improved Holographic QCD. *Phys. Rev. Lett.*, 101:181601, 2008.
- [35] Oliver DeWolfe, Steven S. Gubser, and Christopher Rosen. A holographic critical point. *Phys. Rev. D*, 83:086005, 2011.
- [36] Yan-Qing Zhao, Song He, Defu Hou, Li Li, and Zhibin Li. Phase structure and critical phenomena in two-flavor QCD by holography. *Phys. Rev. D*, 109(8):086015, 2024.
- [37] Musa R. Khan, Ayrton Nascimento, Yumu Yang, Joaquin Grefa, Mauricio Hippert, Jorge Noronha, Claudia Ratti, and Romulo Rougemont. Uncertainty quantification of holographic transport and energy loss for the hot and baryon-dense QGP. 3 2026.
- [38] Christian Ecker, Niko Jokela, and Matti Järvinen. Locating the QCD critical point with input from neutron-star observations. *Phys. Rev. D*, 113(4):L041302, 2026.
- [39] Andreas Karch, Emanuel Katz, Dam T. Son, and Mikhail A. Stephanov. Linear confinement and AdS/QCD. *Phys. Rev. D*, 74(1):015005, 2006.
- [40] Yu-Gang Ma, Long-Gang Pang, Rui Wang, and Kai Zhou. Phase Transition Study Meets Machine Learning. *Chin. Phys. Lett.*, 40(12):122101, 2023.
- [41] Kai Zhou, Lingxiao Wang, Long-Gang Pang, and Shuzhe Shi. Exploring QCD matter in extreme conditions with Machine Learning. *Prog. Part. Nucl. Phys.*, 135:104084, 2024.
- [42] Yongjia Wang and Qingfeng Li. Machine learning transforms the inference of the nuclear equation of state. *Front. Phys. (Beijing)*, 18(6):64402, 2023.
- [43] Long-Gang Pang. Studying high-energy nuclear physics with machine learning. *Int. J. Mod. Phys. E*, 33(06):2430009, 2024.

- [44] Ran Li, Yi-Lun Du, and Shanshan Cao. Deep learning for jet modification in the presence of the quark gluon plasma background. *Phys. Rev. C*, 113(2):024912, 2026.
- [45] Shuzhe Shi. Quantum computation and machine learning in high energy nuclear physics. *J. Subatomic Part. Cosmol.*, 5:100326, 2026.
- [46] Koji Hashimoto, Keisuke Ohashi, and Takayuki Sumimoto. Deriving the dilaton potential in improved holographic QCD from the meson spectrum. *Phys. Rev. D*, 105(10):106008, 2022.
- [47] Xun Chen, Yidian Chen, and Kai Zhou. Data-Driven Einstein-Dilaton Model for Pure Yang-Mills Thermodynamics and Glueball Spectrum. 7 2025.
- [48] Yu Zhang, Xun Chen, and Miguel Angel Martin Contreras. Heavy Quarkonium Spectrum and Decay Constants from a Neural-Network-Based Holographic Model. 1 2026.
- [49] Mathew Thomas Arun and Ritik Pal. Learning holographic QCD with unflavoured meson spectra. 12 2025.
- [50] Hong-An Zeng, Lingxiao Wang, and Mei Huang. HoloNet: Toward a Unified Einstein-Maxwell-Dilaton Framework of QCD. 12 2025.
- [51] Rong-Gen Cai, Song He, Li Li, and Hong-An Zeng. Neural ordinary differential equations for mapping the magnetic QCD phase diagram via holography. *Sci. China Phys. Mech. Astron.*, 69(4):240414, 2026.
- [52] Yutian Deng, Mei Huang, and Lin Zhang. Holographic QCD equation of state constrained by lattice QCD: neural-ODE for probe-limit and a back-reaction test. 2 2026.
- [53] Yu-Kun Yan, Shao-Feng Wu, Xian-Hui Ge, and Yu Tian. Deep learning black hole metrics from shear viscosity. *Phys. Rev. D*, 102(10):101902, 4 2020.
- [54] Koji Hashimoto, Sotaro Sugishita, Akinori Tanaka, and Akio Tomiya. Deep Learning and Holographic QCD. *Phys. Rev. D*, 98(10):106014, 2018.
- [55] Mahdi Mansouri, Kazem Bitaghsir Fadafan, and Xun Chen. Holographic complex potential of a quarkonium from deep learning. 6 2024.
- [56] Ou-Yang Luo, Xun Chen, Fu-Peng Li, Xiao-Hua Li, and Kai Zhou. Neural network modeling of heavy-quark potential from holography. *Eur. Phys. J. C*, 85(6):637, 2025.
- [57] Koji Hashimoto, Sotaro Sugishita, Akinori Tanaka, and Akio Tomiya. Deep learning and the AdS/CFT correspondence. *Phys. Rev. D*, 98(4):046019, 2018.
- [58] Hyun-Sik Jeong, Hanse Kim, Keun-Young Kim, Gaya Yun, Hyeonwoo Yu, and Kwan Yun. AdS/Deep-Learning made easy II: neural network-based approaches to holography and inverse problems. 11 2025.
- [59] Byoungjoon Ahn, Hyun-Sik Jeong, Keun-Young Kim, and Kwan Yun. Holographic reconstruction of black hole spacetime: machine learning and entanglement entropy. *JHEP*, 01:025, 2025.
- [60] Byoungjoon Ahn, Hyun-Sik Jeong, Keun-Young Kim, and Kwan Yun. Deep learning bulk spacetime from boundary optical conductivity. *JHEP*, 03:141, 2024.
- [61] Mugeon Song, Maverick S. H. Oh, Yongjun Ahn, and Keun-Young Kim. AdS/Deep-Learning made easy: simple examples. *Chin. Phys. C*, 45(7):073111, 2021.
- [62] Li-Qiang Zhu, Ou-Yang Luo, Xun Chen, Kai Zhou, Hanzhong Zhang, and De-Fu Hou. Thermodynamics of Heavy Quarkonium in a Bayesian Holographic QCD model. *Nucl. Sci. Tech.*, 37(4):68, 2026.
- [63] Xun Chen and Mei Huang. Machine learning holographic black hole from lattice QCD equation of state. *Phys. Rev. D*, 109(5):L051902, 2024.
- [64] Xun Chen and Mei Huang. Flavor dependent critical endpoint from holographic QCD through machine learning. *JHEP*, 02:123, 2025.
- [65] Xun Chen, Floriana Giannuzzi, and Stefano Nicotri. Data-Driven Refinement of an Analytical Holographic Model for the QCD Phase Transition. 12 2025.
- [66] Anton Andronic, Peter Braun-Munzinger, Krzysztof Redlich, and Johanna Stachel. Decoding the phase structure of QCD via particle production at high energy. *Nature*, 561(7723):321–330, 2018.
- [67] U. Gursoy and E. Kiritsis. Exploring improved holographic theories for QCD: Part I. *JHEP*, 02:032, 2008.
- [68] Danning Li, Song He, Mei Huang, and Qi-Shu Yan. Thermodynamics of deformed AdS₅ model with a positive/negative quadratic correction in graviton-dilaton system. *JHEP*, 09:041, 2011.
- [69] Song He, Shang-Yu Wu, Yi Yang, and Pei-Hung Yuan. Phase Structure in a Dynamical Soft-Wall Holographic QCD Model. *JHEP*, 04:093, 2013.
- [70] Yi Yang and Pei-Hung Yuan. A Refined Holographic QCD Model and QCD Phase Structure. *JHEP*, 11:149, 2014.
- [71] Yi Yang and Pei-Hung Yuan. Confinement-deconfinement phase transition for heavy quarks in a soft wall holographic QCD model. *JHEP*, 12:161, 2015.
- [72] David Dudal and Subhash Mahapatra. Thermal entropy of a quark-antiquark pair above and below deconfinement from a dynamical holographic QCD model. *Phys. Rev. D*, 96(12):126010, 2017.
- [73] D. Dudal and S. Mahapatra. Interplay between the holographic QCD phase diagram and entanglement entropy. *JHEP*, 07:120, 2018.
- [74] Xun Chen, Danning Li, and Mei Huang. Chiral phase transition in the soft-wall model of AdS/QCD. *Chin. Phys. C*, 43(2):023105, 2019.
- [75] Xun Chen, Lin Zhang, Danning Li, Defu Hou, and Mei Huang. Chiral phase transition and magnetic effects in the soft-wall AdS/QCD model. *JHEP*, 07:132, 2020.
- [76] Jianhui Zhou, Xun Chen, Yu-Qiang Zhao, and Jialun Ping. Thermodynamics and phase transitions of holographic QCD in a finite volume. *Phys. Rev. D*, 102(8):086020, 2020.
- [77] Xun Chen, Danning Li, Defu Hou, and Mei Huang. Dynamical holographic QCD model for glueball and light meson spectra. *JHEP*, 03:073, 2020.
- [78] Bin Chen, Xun Chen, Xin Li, Zhi-Rui Zhu, and Kai Zhou. Non-equilibrium dynamics and critical behavior in holographic QCD phase transitions. *Phys. Rev. D*, 111(8):086033, 2025.
- [79] Lingxiao Zhu, Xun Chen, Kai Zhou, Hong Zhang, and Mei Huang. Holographic study of QCD phase diagram with rotation and magnetic field. 2025. To appear.
- [80] Liqiang Zhu, Xun Chen, Kai Zhou, Hanzhong Zhang, and Mei Huang. Bayesian inference of the critical end point in a (2+1)-flavor system from holographic QCD. *Phys. Rev. D*, 112(2):026019, 2025.
- [81] Bing Chen, Liqiang Zhu, Xun Chen, Defu Hou, and Xurong Chen. Transport Properties of QGP within a Bayesian Holographic QCD Model. 8 2025.
- [82] Renato Critelli, Jorge Noronha, Jacquelyn Noronha-Hostler, Israel Portillo, Claudia Ratti, and Romulo Rougemont. Critical point in the phase diagram of primordial quark-gluon matter from black hole physics. *Phys. Rev. D*, 96(9):096026, 2017.

- [83] Yi Yang and Pei-Hung Yuan. Universal Behaviors of Speed of Sound from Holography. *Phys. Rev. D*, 97(12):126009, 2018.
- [84] Meng-Wei Li, Yi Yang, and Pei-Hung Yuan. Analytic Study on Chiral Phase Transition in Holographic QCD. *JHEP*, 02:055, 2021.
- [85] Umut Gursoy, Matti Jarvinen, and Govert Nijs. Holographic QCD in the Veneziano Limit at a Finite Magnetic Field and Chemical Potential. *Phys. Rev. Lett.*, 120(24):242002, 2018.
- [86] R. Bellwied, S. Borsanyi, Z. Fodor, S. D. Katz, A. Pasztor, C. Ratti, and K. K. Szabo. Fluctuations and correlations in high temperature QCD. *Phys. Rev. D*, 92(11):114505, 2015.
- [87] Volodymyr Vovchenko and Horst Stoecker. Thermal-FIST: A package for heavy-ion collisions and hadronic equation of state. *Comput. Phys. Commun.*, 244:295–310, 2019.
- [88] D. Bollweg, J. Goswami, O. Kaczmarek, F. Karsch, Swagato Mukherjee, P. Petreczky, C. Schmidt, and P. Scior. Taylor expansions and Padé approximants for cumulants of conserved charge fluctuations at nonvanishing chemical potentials. *Phys. Rev. D*, 105(7):074511, 2022.
- [89] A. Bazavov et al. The QCD Equation of State to $\mathcal{O}(\mu_B^6)$ from Lattice QCD. *Phys. Rev. D*, 95(5):054504, 2017.
- [90] Yumu Yang, Prachi Garella, Musa R. Khan, Tulio E. Restrepo, Joaquin Grefa, Johannes Jahan, Mauricio Hippert, Jorge Noronha, Claudia Ratti, and Romulo Rougemont. Merging multidimensional equations of state of strongly interacting matter via a statistical mixture. 1 2026.
- [91] Wei-jie Fu, Jan M. Pawłowski, and Fabian Rennecke. QCD phase structure at finite temperature and density. *Phys. Rev. D*, 101(5):054032, 2020.
- [92] Hong Zhang, Defu Hou, Toru Kojo, and Bin Qin. QCD phase diagram with 2+1 flavors using Dyson-Schwinger equations. *Phys. Rev. D*, 96(11):114029, 2017.
- [93] M. Osman, D. Hou, W. Wang, and H. Zhang. *Eur. Phys. J. C*, 85:804, 2025.
- [94] J. V. Roth, Y. Ye, S. Schlichting, and L. von Smekal. *JHEP*, 01:118.
- [95] F. Murgana, V. Greco, M. Ruggieri, and D. Zappalà. *Phys. Rev. D*, 109:096017, 2024.
- [96] P. Isserstedt, M. Buballa, C. S. Fischer, and P. J. Gunkel. *Phys. Rev. D*, 100:074011, 2019.
- [97] Fei Gao and Yu-xin Liu. Phase structure and critical properties in the three-flavor Nambu–Jona-Lasinio model with nonzero temperature and density. *Phys. Rev. D*, 94(7):076009, 2016.
- [98] Si-xue Qin, Lei Chang, Hong Chen, Yu-xin Liu, and Craig D. Roberts. Phase diagram and critical endpoint for strongly-interacting quarks. *Phys. Rev. Lett.*, 106(17):172301, 2011.
- [99] Chao Shi, Yin-li Wang, Yu Jiang, Zhu-fang Cui, and Hong-shi Zong. Further studies on the chiral phase transition in the PNJL model at finite temperature and chemical potential. *JHEP*, 07:014, 2014.
- [100] Christian S. Fischer, Jan Luecker, and Christian A. Welzbacher. Phase structure of three and four flavor QCD. *Phys. Rev. D*, 90(3):034022, 2014.